Bridging the gap between physics and chemistry in early stages of star formation
Nazari, P.

Citation

Nazari, P. (2024, February 13). *Bridging the gap between physics and chemistry in early stages of star formation*. Retrieved from https://hdl.handle.net/1887/3717029

Version:	Publisher's Version
License:	Licence agreement concerning inclusion of doctoral thesis in the Institutional Repository of the University of Leiden
Downloaded from:	https://hdl.handle.net/1887/3717029

Note: To cite this publication please use the final published version (if applicable).

Chapter 8

Importance of source structure on complex organics emission III. Effect of disks around massive protostars

P. Nazari, B. Tabone, and G. P. Rosotti

Abstract

Context. The hot molecular core phase of massive star formation shows emission from complex organic molecules. However, these species are only detected toward a fraction of high-mass protostars. In particular, there is a spread of ∼2 orders of magnitude in methanol emission intensity from high-mass protostars.

Aims. The goal of this work is to answer the question of whether high-mass disks can explain the lack of methanol emission from some massive protostellar systems.

Methods. We considered an envelope-only and an envelope-plus-disk model and used the code RADMC-3D to calculate the methanol emission. High and low millimeter (mm) opacity dust (representing large and small dust distributions) were considered for both models separately, and the methanol abundance was parameterized. Viscous heating was included due to the high accretion rates of these objects in the disk.

Results. In contrast with low-mass protostars, the presence of a disk does not significantly affect the temperature structure and methanol emission. The shadowing effect of the disk is not as important for high-mass objects, and the disk midplane is hot because of viscous heating, which is effective due to the high accretion rates. The methanol emission is lower for models with high mm opacity dust because the dust attenuation blocks the emission in the envelope and hides it in the disk through continuum oversubtraction, but the disk needs to be large for this to become effective. A minimum disk size of ∼2000 − 2500 au is needed (at $L = 10^4\,\mathrm{L_\odot}$) with high mm opacity dust for drop of a factor of about one order of magnitude in the methanol emission compared with the envelope-only models with low mm opacity dust. Consistent with observations of infrared absorption lines toward high-mass protostars, we find a vertical temperature inversion, that is, higher temperatures in the disk midplane than the disk surface, at radii ≲50 au for models with $L = 10^4\,\mathrm{L_\odot}$ and high mm opacity dust as long as the envelope mass is ≳550 M$_\odot$ ($\dot{M} = 3.6 \times 10^{-3}\,\mathrm{M_\odot\,yr^{-1}}$).

Conclusions. The large observed scatter in methanol emission from massive protostars can be mostly explained toward lower-luminosity objects (∼$10^3\,\mathrm{L_\odot}$) with the envelope-plus-disk models including low and high mm opacity dust. The methanol emission variation toward sources with high luminosities (≳ $10^4\,\mathrm{L_\odot}$) cannot be explained by models with or without a disk with a relatively high gas-phase abundance of methanol. However, the luminosity-to-mass ratios of these objects suggest that they might be associated with hypercompact or ultracompact HII regions. Therefore, the low methanol emission toward the high-luminosity sources can be explained by them hosting an HII region in which methanol is absent.

8.1   Introduction

Protostellar systems are the hottest and thus the richest phase of star formation in gaseous complex organic molecules sublimating from the ices (Herbst & van Dishoeck 2009; Caselli & Ceccarelli 2012 Jørgensen et al. 2020; van 't Hoff et al. 2020b). These species are detected toward both low- and high-mass protostars (e.g., Blake et al. 1987; van Dishoeck et al. 1995a; Schilke et al. 1997; Cazaux et al. 2003; Beltrán et al. 2009; Belloche et al. 2013; Jørgensen et al. 2016; Rivilla et al. 2017; Bøgelund et al. 2018; Martín-Doménech et al. 2019; van Gelder et al. 2020; Taniguchi et al. 2020; Gorai et al. 2021). Among these species, methanol is the most abundant and well-studied species, and it is known to mostly form on the surfaces of interstellar dust grains (Watanabe & Kouchi 2002; Fuchs et al. 2009). In this work, we focus on methanol as a representative of complex organic species.

Although many high-mass protostars do show millimeter (mm) emission from methanol, there are many that do not. In particular, van Gelder et al. (2022b) surveyed the methanol mass toward a large number of low- and high-mass protostars (for the low-mass sample, also see Yang et al. 2021 and Belloche et al. 2020). These observations were taken with the Atacama Large Millimeter/submillimeter Array (ALMA). They found a scatter of four orders of magnitude in warm methanol mass. van Gelder et al. (2022b) discussed various reasons for this scatter, including the possible effect of dust optical depth (Rivilla et al. 2017; López-Sepulcre et al. 2017; De Simone et al. 2020) and the presence of a disk (Persson et al. 2016). Nazari et al. (2022b) investigated the effect of a disk and optically thick dust on lowering the mm emission from methanol toward low-mass protostars using radiative transfer modeling. They found that a disk and optically thick dust are both necessary to explain the lack of methanol emission at mm wavelengths in these objects. However, it is not yet clear whether disks can explain this lack of methanol emission toward massive protostars.

A disk around low-mass protostars lowers the emission because it generally decreases the temperature of the environment through disk shadowing and creating a cold midplane (e.g., Murillo et al. 2015). Therefore, methanol molecules are mostly frozen out and are unable to emit in mm wavelengths. Moreover, optically thick dust in the disk causes the continuum oversubtraction effect and decreases the line flux even further (Nazari et al. 2022b). This effect, as explained in detail in Nazari et al. 2022b, occurs when the methanol molecules are on top of the dust in the disk and in between the dusty disk and the observer. Therefore, dust does not block the methanol emission. If the continuum emission is approximately as strong as the methanol emission, it will hide the methanol emission in this scenario, and continuum subtraction will produce an error.

High-mass protostars have much higher accretion rates than low-mass protostars ($\sim 10^{-4} - 10^{-3}\,\mathrm{M_\odot\,yr^{-1}}$; Hosokawa & Omukai 2009; Beuther et al. 2017). This means that viscous heating in the disk midplane becomes important, especially for accretion rates above $\sim 10^{-5}\,\mathrm{M_\odot\,yr^{-1}}$ (Harsono et al. 2015a). Observational evidence of this heating are the mid-infrared absorption lines toward high-mass disks (Knez et al. 2009; Barr et al. 2020). This was interpreted to mean that the colder disk surface absorbs the emission from the hotter gas in the

midplane. Therefore, high-mass protostellar disks may not affect the methanol emission in a manner similar to the low-mass protostellar disks.

Another complication in studying massive protostellar disks is the ongoing debate about the high-mass star formation process. Several theories have been proposed, and two of them are more favored. High-mass stars are thought to either form in the same way as in the low-mass stars (core accretion) or through competitive accretion (Bonnell & Bate 2006; Myers et al. 2013; Tan et al. 2014; Motte et al. 2018). Although both theories suggest the existence of massive protostellar disks, the stability of these disks is debated (Ahmadi et al. 2019; Johnston et al. 2020). On the one hand, many works showed that these massive disks fragment at a radius threshold of ∼100 − 200 au (Kratter & Matzner 2006; Krumholz et al. 2009; Oliva & Kuiper 2020). On the other hand, other studies showed that disks with radii of 1000 au can also form (Kuiper et al. 2010; Kuiper et al. 2011; Klassen et al. 2016; Kuiper & Hosokawa 2018). Interferometric observations showed evidence for disks around massive young stellar objects (Jiménez-Serra et al. 2012; Sánchez-Monge et al. 2013b; Hirota et al. 2014 Hunter et al. 2014; Johnston et al. 2015; Zapata et al. 2015; Ilee et al. 2016; Cesaroni et al. 2017; Maud et al. 2019; Bøgelund et al. 2019a; Williams et al. 2022). Disk masses were found to be around $3 − 12\,\mathrm{M_\odot}$, disk radii around $800 − 2500$ au, and protostellar masses around $20 − 70\,\mathrm{M_\odot}$. Based on these observations, disks around massive protostars seem to be common rather than an exception.

A final difference of high-mass protostars from their low-mass counterparts is that they may host an HII region. HII regions are divided into different categories depending on their extent. In this work, the most relevant categories are the hypercompact (HC) and ultracompact (UC) HII regions. They are defined to have an extent of $\lesssim 10300$ au (Kurtz 2005; Hoare et al. 2007) and $\lesssim 20600$ au (Wood & Churchwell 1989; Hoare et al. 2007), respectively. Therefore, the effect of these regions needs to be considered.

In this paper, we address the question of whether massive protostellar disks and optically thick continuum can explain the lack of methanol emission toward high-mass protostars. To answer this question, we study an envelope-only and an envelope-plus-disk model following a similar method to Nazari et al. (2022b). We calculate the temperature and methanol emission by detailed radiative transfer modeling. For both models, we consider optically thin and thick dust at mm wavelengths and parameterize the methanol abundance in the disk and the envelope.

The main difference between the models in Nazari et al. (2022b) and those in this work is the viscous heating that is included in the disk of high-mass protostars, while this was not considered in Nazari et al. (2022b). Moreover, the region of the parameter space that this work considers includes higher envelope masses and protostellar luminosities to match those of observations of high-mass protostellar systems.

In Sect. 8.2 we summarize our methods. Section 8.3 presents the results, in particular, the effect of a disk on the temperature structure and the resulting methanol emission. Moreover, we explore the temperature inversion effect suggested by Barr et al. (2020). We discuss our findings in Sect. 8.4. Our results are

in particular compared with observations, and the effect of HII regions is discussed. Finally, we present our conclusions in Sect. 8.5.

8.2   Methods

8.2.1   Physical structure and abundance

We considered two models: an envelope-only model, and an envelope-plus-disk model. The two models have the same physical structure as in Nazari et al. (2022b) , and thus their details are only briefly stated here. The gas density structures of the two models are presented in Fig. 1. The envelope-only model has a power-law relation between gas density and radius (in spherical coordinates r) with its power fixed to -1.5 (i.e., $\rho_{\rm g} \propto r^{-1.5}$). This value was chosen to be consistent with observations of massive protostellar envelopes (van der Tak et al. 2000; Gieser et al. 2021). The envelope-plus-disk model consists of a flattened-envelope density structure with an embedded disk. The flattened-envelope model has a gas density structure following Ulrich (1976). The disk density follows a power law in (cylindrical) R and a Gaussian profile in z direction (Shakura & Sunyaev 1973; Pringle 1981). We assumed a disk aspect ratio (H/R) of 0.2 similar to Nazari et al. 2022b (also see Harsono et al. 2015a). A gas-to-dust mass ratio of 100 was assumed for both models. An outflow cavity was carved for both models in the same way as done in Nazari et al. (2022b). The outflow cavity had a curved opening with total hydrogen nucleus number density fixed to $10^3 \, \mathrm{cm}^{-3}$, where $\cos \theta_0 > 0.95$. Here θ_0 is the latitude of the particle at its initial location in the envelope. The curved opening angle is important for UV penetration into the envelope (Bruderer et al. 2009).

Envelope masses of the modeled protostars were varied between $50 \, \mathrm{M}_\odot$ and $1000 \, \mathrm{M}_\odot$ following single-dish observations of the extended envelopes (van der Tak et al. 2000; van der Tak et al. 2013; Benz et al. 2016; König et al. 2017; Pitts et al. 2022). The bolometric luminosities were varied between $5 \times 10^2 \, \mathrm{L}_\odot$ and $5 \times 10^6 \, \mathrm{L}_\odot$ (e.g., see Lumsden et al. 2013; Elia et al. 2017 for the observed values for high-mass objects). We note that the luminosity range and envelope mass range assumed here include the range that is often referred to as intermediate-mass protostars ($L \lesssim 10^4 \, \mathrm{L}_\odot$ and $M_{\rm E} \lesssim 100 \, \mathrm{M}_\odot$). However, we kept these values for completeness. The disk radii for the envelope-plus-disk models span a range between $300 \, \mathrm{au}$ and $2500 \, \mathrm{au}$ following the disks observed around O- and B-type protostars (Hunter et al. 2014; Johnston et al. 2015; Ilee et al. 2016; Ilee et al. 2018; Zhang et al. 2019; Sanna et al. 2019; Añez-López et al. 2020). The disk masses were varied such that $M_{\rm D}/R_{\rm D}^2$ stayed constant. The disk mass for the fiducial model with disk radius of $1000 \, \mathrm{au}$ was assumed as $3 \, \mathrm{M}_\odot$ (resulting in a disk mass range of $\sim 0.3 - 19 \, \mathrm{M}_\odot$). This value was chosen to be consistent with the observed massive disks around O- and B-type protostars (references given above). The central protostar mass and temperature were fixed to $30 \, \mathrm{M}_\odot$ and $40000 \, \mathrm{K}$. In Sect. 8.4.3 we discuss the effect of changing the protostar mass and temperature on the methanol emission. The outer radius of the envelope was fixed to $5 \times 10^4 \, \mathrm{au}$ (van der Tak et al. (2000); Shirley et al. 2002; Pitts et al. 2022).
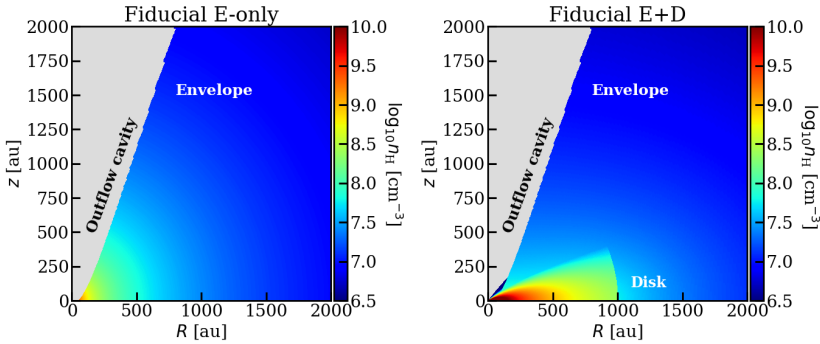
Figure 8.1: Gas density profiles. Two-dimensional total hydrogen nucleus number density for the fiducial envelope-only model (left). The same, but for the fiducial envelope-plus-disk model (right). The outflow cavities in this and subsequent figures are masked gray.

The inner radius was taken to be 10 au. However, because the temperature for some models (especially those with the highest luminosities) at radii between 10 au and 20 au exceeds 2000 K (upper limit on the dust sublimation temperature), the methanol abundance was set to zero in the inner 20 au. This assumption does not change the integrated methanol flux considered in the paper. All these parameters are summarized in Table 8.1. We did not include an HII region in our models. However, its effect on methanol emission is discussed in Sect. 8.4.2.2. The fiducial envelope-only and envelope-plus-disk models throughout this work are defined to be those with M_{env} of 300 $M_\odot$, L of 10^4 $L_\odot$, R_D of 1000 au, and M_D of 3 $M_\odot$ with small $\kappa_{\mathrm{dust,\,mm}}$ (see the highlighted values in Table 8.1).

Methanol abundances in the disk and the envelope were calculated by balancing adsorption and thermal desorption (Hasegawa et al. 1992). The binding energy of methanol was assumed to be 3820 K (Penteado et al. 2017). The total methanol abundance ($X_{\mathrm{gas}} + X_{\mathrm{ice}}$) with respect to total hydrogen in the envelope was taken to be 10^{-6}, with a minimum of 10^{-9} outside of the snow surface for X_{gas}, following what Nazari et al. (2022b) used for low-mass protostars (also see Drozdovskaya et al. 2015). This is justified given that the methanol-ice abundances of low- and high-mass young stellar objects with respect to hydrogen are similar (Öberg et al. 2011; Boogert et al. 2015). In the disk, the total ice and gas abundance of methanol was assumed to be 10^{-8} with a minimum of 10^{-11} for X_{gas}. These values are based on the modeling and observational works of low-mass protostars (Walsh et al. 2014; Booth et al. 2021) and mimic the potential effect from shocks that can destroy methanol. We note that the methanol abundance found by Bøgelund et al. (2019a) in the envelope/disk of AFGL 4176 is $\sim 10^{-5} - 10^{-6}$. This value could be overestimated because of continuum optical thickness. However, we explore higher assumed disk abundances in Sect. 8.4.3 and explain its effect on methanol emission. In our models, chemical evolution of methanol in the disk and envelope was not included directly to focus on the effect of disk on methanol emission. These effects,

Table 8.1: Model parameters

Parameter [unit]	Envelope-only	Envelope-plus-disk	Description
r_{in} [au]	10	10	The inner radius
r_{out} [au]	5×10^4	5×10^4	The outer radius of the envelope
M_{E} [M$_\odot$]	50, 150, **300**, 550, 800, 1000	50, 150, **300**, 550, 800, 1000	Envelope mass
R_{D} [au]	–	300, 500, **1000**, 1500, 2000, 2500	Disk radius
M_{D} [M$_\odot$]	–	0.27, 0.75, **3.** , 6.75, 12. , 18.75	Disk mass
$\dot{M}$ [M$_\odot$ yr^{-1}]	–	3.3×10^{-4}, 9.8×10^{-4}, **2.0$\times 10^{-3}$**, 3.6×10^{-3}, 5.2×10^{-3}, 6.5×10^{-3}	Mass accretion rate
$T_\star$ [K]	40000	40000	Protostellar temperature
$M_\star$ [M$_\odot$]	30	30	Protostellar mass
L [L$_\odot$]	5×10^2, 5×10^3, **10^4**, 5×10^4, 5×10^5 , 5×10^6	5×10^2, 5×10^3, **10^4**, 5×10^4, 5×10^5 , 5×10^6	Bolometric luminosity

Notes. Parameters of the fiducial model are highlighted with bold face. The disk masses were varied such that $M_{\mathrm{D}}/R_{\mathrm{D}}^2$ (an approximation to the disk surface density) stayed constant, assuming a fiducial disk mass of 3 M$_\odot$. The centrifugal radius was fixed to 500 au (see Eq. 2 in Nazari et al. 2022b for its effect).

however, are included implicitly by parameterizing the methanol abundance based on the previous observations and chemical models. Further effects from chemical evolution are discussed in Sect. 8.4.

The photodissociation regions of methanol around the cavity walls were calculated in the same way as Nazari et al. (2022b). In short, we assumed that methanol is photodissociated in the regions alongside the outflow cavity wall, where $\tau_{UV} < 3$, and hence, its abundance was set to zero in these regions. The opening angle for the outflow cavity considered here is ~20 degrees narrower than that in Bruderer et al. (2009). However, as discussed in Bruderer et al. (2009, 2010), the warm ($T > 100$ K) mass only changes by less than a factor of 3 for different cavity shapes and opening angles. Moreover, our photodissociation regions (where $\tau_{UV} < 3$) for the low mm opacity dust grains have a similar extent as those in Bruderer et al. (2009) (see Fig. 8.B.4 and their Fig. 3).

8.2.2   Temperature calculation

We used the code RADMC-3D (Dullemond et al. 2012) version 2.0[1] to calculate the dust temperature in the envelope and the disk. The same two dust distributions as Nazari et al. (2022b) were considered (see their Appendix A for κ_{abs} as a function of wavelength). One distribution with $\kappa_{1\,mm} \simeq 0.2\,\mathrm{cm^2\,g^{-1}}$ and the other with $\kappa_{1\,mm} \simeq 18\,\mathrm{cm^2\,g^{-1}}$, to include the two extreme cases of low and high dust opacity at mm wavelengths, representing small and large grains, respectively. The two dust distributions are referred to as low mm opacity and high mm opacity dust for the rest of this work.

The grids for both envelope-only and envelope-plus-disk models were logarithmically spaced with 1000 and 400 grid points in the r and θ direction, respectively. Moreover, 10^6 photons were used for the temperature calculation. The number of grid cells and photons was chosen to produce accurate temperatures while maintaining a reasonable computation time.

The models are exactly the same in this work and in Nazari et al. (2022b), except for the viscous heating that is included in the disk for high-mass protostars here (also see Harsono et al. 2015a for viscous heating included in low-mass protostellar disks) and the stellar spectrum we assumed. These two differences are explained below.

We included viscous heating because massive disks have high accretion rates (Beuther et al. 2017). Starting from the disk gas surface density steady-state solution, we can write viscosity as (Pringle 1981; Lodato 2008)

$$\nu = \frac{\dot{M}}{3\pi\Sigma} \left(1 - \sqrt{\frac{R_{in}}{R}} \right), \tag{8.1}$$

where Σ is the gas surface density, $\dot{M}$ is the accretion rate, R is the radius in cylindrical coordinates, and R_{in} is the inner radius of the disk.

---

[1]`http://www.ita.uni-heidelberg.de/~dullemond/software/radmc-3d`

The viscous torques are important for angular momentum transfer throughout the disk to allow accretion, but they also cause energy to be dissipated. The power lost per unit volume by the viscous torques in the disk can be found using

$$Q(R, z) = \frac{-G(R, z)\Omega'}{2\pi R},$$

(8.2)

where $G(R, z)$ is the torque exerted by viscosity per unit length, and Ω' is $d\Omega/dR$, with Ω being the angular velocity. The torque per length is given by

$$G(R, z) = -2\pi\nu\rho R^3 \Omega'.$$

(8.3)

We can substitute ν from Eq. (8.1) into Eq. (8.3) and then substitute the resulting $G(R, z)$ into Eq. (8.2) to find the power that is dissipated by viscosity per unit volume as

$$Q(R, z) = \frac{3}{4\pi} \frac{\dot{M}\rho\Omega^2}{\Sigma} (1 - \sqrt{\frac{R_{in}}{R}}).$$

(8.4)

This expression was found for each grid cell and was included as an additional heating source in the temperature calculation of RADMC-3D. Although the viscous torque (Eq. 8.3) depends on ν, this itself depends on the mass accretion rate. We assumed that the disk is viscous enough to deliver the entire accretion rate it receives from the envelope, and there is no pile-up of material at the envelope-disk intersect. Hence, Eq. (8.4) only depends on the mass accretion rate. In other words, we did not vary ν directly, but by varying $\dot{M}$, we took various viscous torques into account. Therefore, we only refer to the mass accretion rate in our models. The mass accretion rate is calculated self-consistently for the density profile and the parameters considered ($\dot{M}[\mathrm{M_\odot yr^{-1}}]/(2 \times 10^{-3}) \simeq \mathrm{M_{env}}[\mathrm{M_\odot}]/300$). The accretion rates are between $3.3 \times 10^{-4}\,\mathrm{M_\odot\,yr^{-1}}$ and $6.5 \times 10^{-3}\,\mathrm{M_\odot\,yr^{-1}}$ in this work.

The stellar spectra with the luminosities given in Table 8.1 are not simple blackbodies, as assumed in Nazari et al. (2022b). This is because the central massive protostar has an effective temperature of 40000 K, and hence, ~40% of the photons in the stellar blackbody spectrum will ionize hydrogen. Because in reality, these photons will be absorbed by the hydrogen atoms before any direct contact with dust and are later reradiated at longer wavelengths, we altered the blackbody spectrum to simulate this effect. We assumed that these photons are later reemitted at the Lyman-α wavelength with a width of $18\,\mathrm{km\,s^{-1}}$ for a Gaussian profile (FWHM = $2\sqrt{2\ln 2} \times 18$). This is approximately equal to the line width found from thermal broadening at temperature of 40000 K. We discuss the effect of completely removing the ionizing photons from the stellar blackbody as a case producing a lower limit on methanol emission in Sect. 8.4.3.

8.2.3   Calculating the line emission

The line emission was calculated using the code RADMC-3D version 2.0. The molecular data were taken from the Leiden Atomic and Molecular Database (downloaded on 16 February 2022; Schöier et al. 2005; van der Tak et al. 2020). The

line properties such as frequency, upper energy level ,and Einstein A coefficient were taken from the Cologne Database for Molecular Spectroscopy (CDMS; Müller et al. 2001; Müller et al. 2005). We calculated the emission from one of the strong methanol lines covered in the ALMA Evolutionary study of High Mass Protocluster Formation in the Galaxy (ALMAGAL) survey (van Gelder et al. 2022b) to be able to compare our results with these observations. The chosen methanol transition has J K L M - J K L M quantum numbers equal to 4 2 3 1-3 1 2 1 and has a frequency of 218.4401 GHz ($E_{\rm up} = 45.5$ K, $A_{\rm i,j} = 4.7 \times 10^{-5}\,{\rm s}^{-1}$). Because this line has a similar upper-state energy and Einstein A coefficient to the line used in Nazari et al. (2022b), where the assumption of local thermodynamic equilibrium (LTE) was found to be valid, we assumed LTE conditions. This is well justified since the densities we considered are even higher than in the low-mass case.

We performed the ray tracing in the same way as Nazari et al. (2022b) with a spectral resolution of $0.2\,{\rm km\,s^{-1}}$. The source was assumed to be located at a distance of 4 kpc (typical distance of high-mass protostars; e.g., Mège et al. 2021). Gas and dust were included in ray tracing, and subsequently, the lines were continuum subtracted before we calculated the integrated line fluxes. The emission was integrated over a $2''$ area. This corresponds to a source diameter of 8000 au for a source located at 4 kpc. The $2''$ was chosen to simulate the angular resolution of surveys of massive protostars such as ALMAGAL, and is large enough to include the disk and the hot core region, where methanol is sublimated for most models. The models with the highest luminosities considered are often hot enough to sublimate methanol up to the outer radii assumed here.

In the envelope, we assumed a turbulent velocity of $2\,{\rm km\,s^{-1}}$ (slightly higher than what was assumed in Nazari et al. 2022b for low-mass protostars, $1\,{\rm km\,s^{-1}}$). This turbulent velocity produces a line emission with a full width at half maximum (FWHM) of $\sim$4 km s^{-1}. The FWHMs of lines toward high-mass protostars are larger than their low-mass counterparts on average (e.g., Nazari et al. 2021; Nazari et al. 2022a). In the disk, a turbulent velocity of $0.1\,{\rm km\,s^{-1}}$ and Keplerian velocity were assumed. Because double-peaked line profiles for methanol are not regularly observed, no free-fall velocity was assumed in the envelope. As discussed in Nazari et al. (2022b), the inclusion of free-fall velocity is not expected to change the main conclusions when we focus on integrated line fluxes.

8.3 Results

In this section, we explain the main results. Most importantly, we discuss the temperature structure and the resulting methanol emission.

8.3.1 Temperature

8.3.1.1 General structure

Figure 8.2 shows the temperature structure of the fiducial ($M_{\rm env} = 300\,{\rm M}_\odot$, $L = 10^4\,{\rm L}_\odot$, $R_{\rm D} = 1000$ au, and $M_{\rm D} = 3\,{\rm M}_\odot$ with small $\kappa_{\rm dust,\,mm}$) envelope-only and envelope-plus-disk models along with those with large $\kappa_{\rm dust,\,mm}$. The temperatures
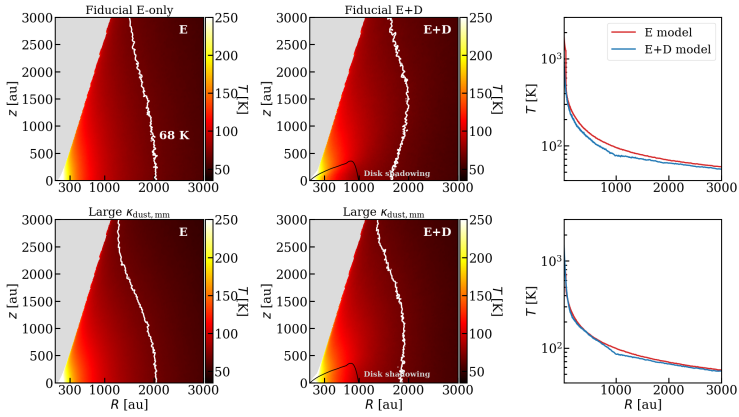
Figure 8.2: Temperature structure of the fiducial envelope-only and envelope-plus-disk. The top row shows the models with low mm opacity dust ($\kappa_{1\,\mathrm{mm}} \simeq 0.2\,\mathrm{cm}^2\,\mathrm{g}^{-1}$), and the bottom row shows models with high mm opacity dust ($\kappa_{1\,\mathrm{mm}} \simeq 18\,\mathrm{cm}^2\,\mathrm{g}^{-1}$). The right column shows a temperature cut for the various models at $z = 0$ au. The white contours show where the temperature is 68 K (roughly where methanol sublimates from the grains). The black contours show the approximate position of the disk.

found in the disk ($\sim 150 - 200\,\mathrm{K}$) agree with what has been observed and assumed previously for disks of massive protostars (Johnston et al. 2015; Izquierdo et al. 2018; Maud et al. 2019). The effect of shadowing behind the disk is observed when the dust has low and high mm opacity. However, this phenomenon does not have as strong an effect on the temperature structure as for low-mass protostars (Nazari et al. 2022b) for the envelope mass and luminosity of the fiducial model. Moreover, the disk midplane is hot due to viscous heating, which is in contrast to the case of low-mass protostars (Nazari et al. 2022b). It is important to note that viscous heating is only effective in changing the temperature structure in the most inner radii ($\lesssim 100$ au; also see Sect. 8.3.1.3). These result in similar temperature structures between models with and without a disk, while the models with a disk have slightly lower temperatures due to disk shadowing (see where the white contours cross the x-axis in Fig. 8.2).

There is little temperature difference between the low mm opacity dust (top row) and high mm opacity dust (bottom row) of Fig. 8.2. Toward $z = 0$ au (midplane), the envelope-plus-disk model has higher temperatures when the dust has large κ_{mm} (compare the white contours in the middle column). This is surprising at first because from the findings of Nazari et al. (2022b), it is expected that the high mm opacity dust absorbs UV and optical light poorly and hence is colder than low mm opacity dust. Moreover, once they absorb the UV and optical photons, they reemit more efficiently at longer wavelengths, which makes the region colder again. However, this is not what is seen here, which is more apparent in the disk midplane.

In the envelope-plus-disk models, this is because of the balance between viscous

heating increasing the temperature in the model with high mm opacity dust, and the effects mentioned above (low κ_{UV} plus high κ_{mm}) lower the temperature in the same model. When viscous heating is included in the disk, the temperature of optically thick regions of the disk (i.e., the dense midplane) depend on the dust optical depth (D'Alessio et al. 1998). When viscous heating is included, the disk midplane is therefore hotter than its surface by a factor $\sim \left(\frac{3}{4}\tau\right)^{1/4}$, where τ is the dust optical depth, which is proportional to the Rosseland mean opacity over wavelengths longer than $\sim 0.1\,\mu$m (see Appendix 8.A; D'Alessio et al. 1998; Armitage 2010). Therefore, the midplane temperature should be higher than the low mm opacity dust for the dust distribution with high mm opacity (which also has a higher Rosseland mean opacity). This is shown with the white contours in the middle panel of Fig. 8.2.

8.3.1.2 Heating sources

There are two sources of heating in our envelope-plus-disk models: radiation from the star (passive heating), and heating due to viscosity. In this section, we quantify the effect from the two heating sources and compare the analytical solutions with the results from RADMC-3D models. Appendix 8.A presents the formulae for calculating viscous heating and passive heating in the disk.

The left panel of Fig. 8.3 presents a comparison between the results from RADMC-3D, the analytical disk midplane temperature profile that results from viscous heating ($T_{\mathrm{mid, visc}}$; Eq. 8.8), and that from passive heating ($T_{\mathrm{mid,irr}}$; Eq. 8.6). The RADMC-3D results and the analytical solutions match well. The temperature profile in the inner disk is explained by viscous heating and that in the outer regions by passive heating. In particular, there is a radius threshold at which $T_{\mathrm{mid,visc}}$ (dashed lines) crosses $T_{\mathrm{mid,irr}}$ (solid black line). This radius is ~ 200 au for the models shown in the left panel of Fig. 8.3. Inside this radius, the contribution from viscous heating is larger than that of passive heating in the disk midplane. Quantitatively, there is a difference of a factor of about 2 between the temperature resulting from viscous heating and that from passive heating at radii of around 10 au for the high mm opacity dust.

The right panel of Fig. 8.3 presents the relation between mass accretion rate and the threshold radius described above, calculated from the analytical formulae given in Appendix 8.A. This threshold can be found by equating $T_{\mathrm{mid, irr}}$ in Eq. (8.6) and $T_{\mathrm{mid, visc}}$ from Eq. (8.8) . Figure 8.3 shows that increasing the mass accretion rate will increase the radius inside which viscous heating is dominant. In other words, for lower-mass envelopes or disks around lower-mass stars (i.e., lower accretion rates), viscous heating is only effective in the inner regions of the disk ($\lesssim 100$ au), as expected from Eq. (8.4) (D'Alessio et al. 1998; Harsono et al. 2015a). More quantitatively, there is a difference of a factor $\gtrsim 2$ in threshold radius between the models with a mass accretion rate of $\sim 3.6 \times 10^{-3}\,\mathrm{M}_\odot\,\mathrm{yr}^{-1}$ and $\sim 3 \times 10^{-4}\,\mathrm{M}_\odot\,\mathrm{yr}^{-1}$.
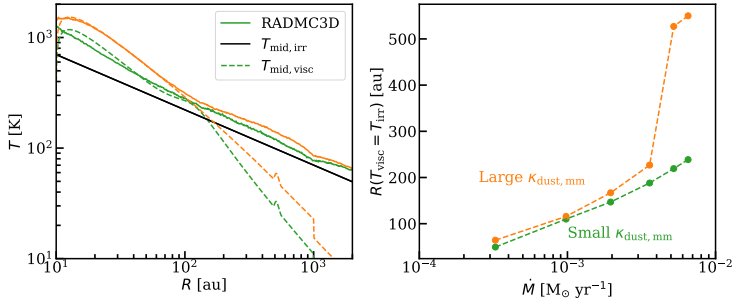
Figure 8.3: Comparison of the midplane temperature calculated by RADMC-3D for the fiducial envelope-plus-disk model (left; solid orange and green lines), and the same calculated from viscous heating analytically (dashed lines) and found from passive heating from the protostar analytically (solid black line). Green shows dust with small κ_{mm}, and orange shows dust with large κ_{mm}. Radius at which the analytical midplane temperature from viscous heating equals that from passive heating, plotted against the mass accretion rate for the fiducial model and for the model with high mm opacity dust (right).

8.3.1.3 Vertical temperature inversion

High-mass protostellar disks have high accretion rates, resulting in viscous heating in the disk. In particular, Sect. 8.3.1.2 explains and Fig. 8.3 shows where in the disk midplane viscous heating is a more dominant source of heating than passive heating from the protostar. However, it is not clear whether viscous heating will cause higher temperatures in the disk midplane than the disk surface. Observations of mid-infrared absorption lines of CO, CS, HCN, C_2H_2, and NH_3 toward the inner radii of the potential disks around AFGL 2136 and AFGL 2591 suggest that the disk surface is colder than the disk midplane (Barr et al. 2020). In this section, we explore this idea and investigate whether a temperature inversion like this is observed in our models.

Figure 8.4 presents vertical cuts for the fiducial envelope-plus-disk model with varying envelope masses (i.e., accretion rates) and the same with large $\kappa_{\mathrm{dust,\,mm}}$. These cuts were made at $\sim$50 au, which is the radius at about which Barr et al. (2020) find that the absorption lines originate. In Fig. 8.4 the outflow cavity wall starts at $z \simeq 50 - 60$ au, indicating where the top surface of the disk or envelope is. With these models, a higher temperature at $z = 0$ au than the temperature just before hitting the cavity wall (i.e., $z \simeq 50 - 60$ au) is needed for a vertical temperature inversion. The left panel of Fig. 8.4 shows that for none of the accretion rates considered here is a temperature inversion like this observed when the dust has a low mm opacity (i.e., small dust). In other words, the temperature in the midplane is always lower than the disk surface when the grains have low $\kappa_{\mathrm{dust,\,mm}}$. We note that the slight decrease in temperature seen (between $z = 0$ au and $z \simeq 30$ au) in left panel of Fig. 8.4 is not enough for observations of absorption lines because the temperature at $z = 0$ au is still lower than that at $z \simeq 60$ au.

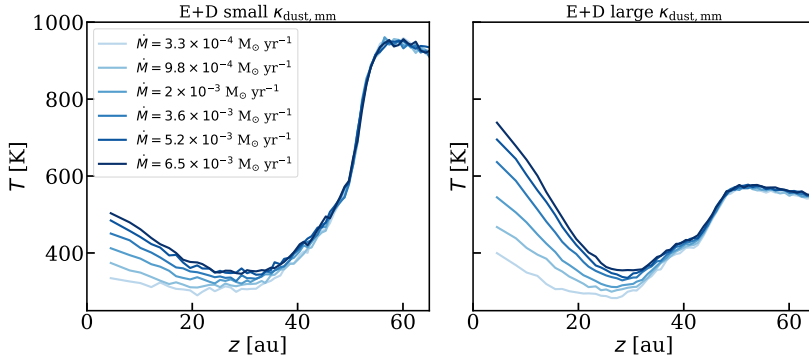The right panel of Fig. 8.4 shows that for a large dust distribution with high

Figure 8.4: Vertical temperature cut at a radius of ~ 50 au. Left: Fiducial envelope-plus-disk model with varying envelope masses and thus various mass accretion rates. Right: Same as in the left panel, but for the fiducial models with large $\kappa_{\mathrm{dust,\,mm}}$. The z of $\sim 50-60$ au marks approximately where the outflow cavity wall and hence the highest z at the disk or envelope surface at a radius of ~ 50 au is reached.

mm opacity, the temperature inversion occurs when the mass accretion rate is at least $\sim 3.6 \times 10^{-3}\,\mathrm{M_\odot\,yr^{-1}}$. Therefore, a source with $R_\mathrm{D} = 1000$ au, $L = 10^4\,\mathrm{L_\odot}$ and high mm opacity dust distribution needs at least an envelope mass of $\sim 550\,\mathrm{M_\odot}$ ($M_\mathrm{env}\,[\mathrm{M_\odot}] \simeq 300/(2 \times 10^{-3})\,\dot{M}\,[\mathrm{M_\odot yr^{-1}}]$) to show higher temperatures in the disk midplane than at the disk surface at a disk radius of 50 au. Based on these results, the models with high mm opacity dust reproduce the vertical temperature inversion suggested by the observations of Barr et al. (2020) better and hence might be more realistic. For sources with accretion rates $\gtrsim 5.2 \times 10^{-3}\,\mathrm{M_\odot\,yr^{-1}}$, the difference between the temperature in the midplane and the disk surface is $\sim 100\,\mathrm{K}$ at least. This can differ when luminosities different from $L = 10^4\,\mathrm{L_\odot}$ are considered or when the temperature cut is made at a radius different than 50 au.

Figure 8.5 shows a two-dimensional temperature map of the fiducial envelope-plus-disk model, but with high mm opacity dust and a mass accretion rate of $5.2 \times 10^{-3}\,\mathrm{M_\odot\,yr^{-1}}$. This figure shows more clearly that the disk mid-plane temperature is hotter than that in the disk surface and envelope at radii below $\sim 50-60$ au.

This phenomenon can be quantified further by comparing the analytical relations of the midplane and surface temperatures of a disk. In Sect. 8.3.1.2 we discussed the analytical formulae for the midplane temperature (Eq. 8.10). The analytical relation for the disk surface temperature from viscous heating (Eq. 8.7) and passive heating (Eq. 8.11) is also given in Appendix 8.A. Therefore, using the total temperature in the midplane (Eq. 8.10) and that at the disk surface (Eq. 8.13), we can find the maximum radius (R_max) at which the temperature in the midplane is higher than that at the disk surface. This radius is dependent on the values of Rosseland mean opacity (κ_R) and Planck mean opacity (κ_P), which change as a function of radius. Therefore, an exact relation for R_max cannot be found, and it needs to be solved numerically. However, assuming typical values
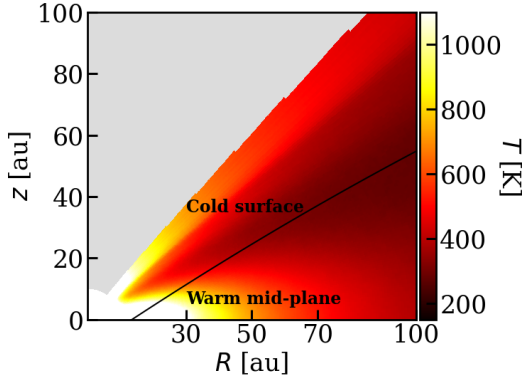
Figure 8.5: Two-dimensional map of the temperature for the fiducial envelope-plus-disk model, but with the difference that this model has high mm opacity dust and an envelope mass of $800\,\mathrm{M_\odot}$ ($\dot{M} = 5.2 \times 10^{-3}\,\mathrm{M_\odot\,yr^{-1}}$). The black contour shows the approximate location of the disk. In the inner disk ($R \lesssim 50 - 60\,\mathrm{au}$), the midplane temperature is higher than the disk surface and envelope temperature.
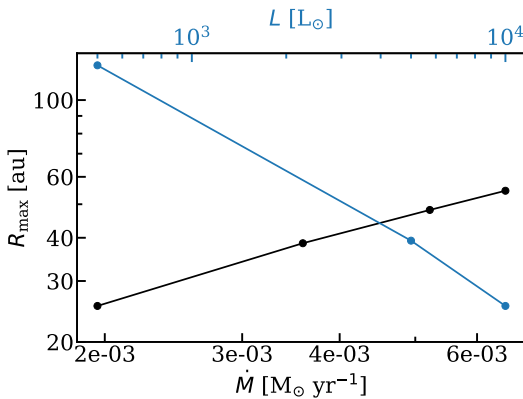

Figure 8.6: Maximum radius at which the midplane temperature is higher than the surface temperature as a function of mass accretion rate (black) and luminosity (blue). The models shown here are fiducial envelope-plus-disk models with large grains (i.e., high mm opacity dust), where M_E ($\dot{M}$) changes for the black line and L changes for the blue line.

of $\sim$60 and $\sim$0.2 (when dust grains have high mm opacity) for τ and ϵ , which depend on κ_{R} and κ_{P} (see Appendix 8.A for the complete definition) between radii of $\sim$50 au and $\sim$100 au, a simple approximate relation for $R_{\max}$ can be found,

$$R_{\max} \simeq \frac{3\dot{M}GM_{\star}\epsilon}{L(1-\epsilon\varphi)}(\frac{3}{4}\tau - 1). \tag{8.5}$$

Here, φ is the flaring angle. This relation only gives a very rough estimate of $R_{\max}$ because τ for the fiducial model but with large dust grains varies between $\sim$45 and $\sim$90 for radii between $\sim$50 au and $\sim$100 au. Moreover, these values would be different for the models with various $\dot{M}$ and L.

Figure 8.6 presents $R_{\max}$ as a function of mass accretion rate (bottom axis in black) and luminosity (top axis in blue) for models with large grains (high mm opacity dust). In this figure, $R_{\max}$ is calculated numerically with values for the mean opacities found iteratively, as explained in Appendix 8.A. At accretion rates below $\sim$2 $\times$ 10^{-3} M$_{\odot}$ yr^{-1} and luminosities above $\sim$10^4 L$_{\odot}$, there is no radius (larger than the inner radius used in the models, i.e., 10 au) at which the midplane temperature is higher than the surface temperature. The same holds for all the models with low mm opacity dust grains. In this figure, the temperature inversion only occurs for the models with high mm opacity dust (also seen in Fig. 8.4) because the disk midplane temperature is proportional to the dust optical depth and thus to the Rosseland mean opacity (see Appendix 8.A). Therefore, the temperature in the disk midplane is higher for the high mm opacity dust (which has a higher Rosseland mean opacity) than that for the low mm opacity dust.

In Fig. 8.6, the maximum radius at which the temperature inversion occurs increases with increasing mass accretion rate. This is because viscous heating is proportional to $\dot{M}$ (see Eq. 8.4). Moreover, this maximum radius decreases as luminosity increases. This is because the increase in the disk surface temperature by passive heating (Eq. 8.11) is steeper than the increase in the disk midplane temperature by passive heating (Eq. 8.6) as luminosity increases.

The black line in Fig. 8.6 shows that an accretion rate of at least $\sim$2 $\times$ 10^{-3} M$_{\odot}$ yr^{-1} is needed for the temperature inversion. At accretion rates below this value, there is no radius (above 10 au) at which the midplane temperature is higher than the surface temperature. Moreover, this inversion only occurs up to radii of $\sim$30 au in the disk. In addition, the results from this figure are in line with those from the right panel of Fig. 8.4. For example, Fig. 8.6 implies that for the temperature inversion to occur at radii of $\sim$40 $-$ 50 au, an accretion rate of at least $\sim$3.6 $\times$ 10^{-3} M$_{\odot}$ yr^{-1} is needed, which is the same as what was found from right panel of Fig. 8.4. Moreover, for luminosities above $\sim$10^4 L$_{\odot}$, no radius (above 10 au) is found at which the temperature inversion occurs, which is also seen in our models (see Fig. 8.B.1).

A caveat in this analysis is the decoupling of gas and dust temperature, which is not considered here. The gas temperature is expected to be higher than dust temperature in the disk surface because of the heating of the gas related to photo-processes, for instance (Kamp & Dullemond 2004; Jonkheid et al. 2004; Bruderer et al. 2012). Therefore, the gas temperature in the midplane in reality needs to be even higher than presented here for vertical temperature inversion to occur. This
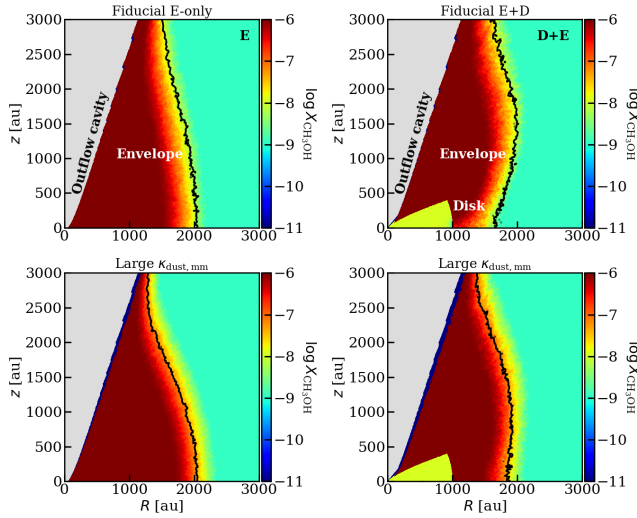
Figure 8.7: Gas-phase methanol abundance map for the fiducial envelope-only and envelope-plus disk models (top row) and those with high mm opacity dust (bottom row). The black contours show the 68 K lines at which methanol starts to be sublimated from the grains at the densities of these models.

implies that high mm opacity dust models are more relevant and closer to reality than those with low mm opacity dust. To conclude, Figures 8.4 and 8.6 show that the temperature inversion occurs in many of our models, especially in those with large grains (i.e., high mm opacity dust). Therefore, a large area of the parameter space explored here agrees with the conclusions of Barr et al. (2020).

8.3.2 Warm methanol mass and its emission

Figure 8.7 presents a methanol abundance map for our fiducial models and those with high mm opacity dust. Methanol is sublimated from the grains throughout the entire disk in our fiducial envelope-plus-disk model and in that with large mm opacity dust grains.

Moreover, the photodissociation regions next to the outflow cavity walls do not exist for the fiducial models, and they are very thin in the fiducial models with high mm opacity dust due to high envelope densities. The photodissociation regions in low-mass protostars of Nazari et al. (2022b) had an important effect in lowering the methanol mass and hence its emission toward low-mass protostars. However, smaller photodissociation regions were seen in low-mass protostars with envelope masses $\gtrsim 3\,M_\odot$ in Nazari et al. (2022b) (see their Fig. E.3) due to the higher densities. Therefore, the photodissociation regions are expected to be smaller for high-mass protostars with higher envelope masses and densities than those in low-mass protostars.

For completeness, Fig. 8.B.2 presents the resulting methanol emission and

continuum-subtracted line fluxes for the fiducial models. Due to the higher turbulent velocity, the FWHMs of the lines are larger ($\sim 4\,\mathrm{km\,s^{-1}}$) than the low-mass protostars in Nazari et al. (2022b) ($\sim 2\,\mathrm{km\,s^{-1}}$). The line emission has a higher peak (by a factor ~ 1.6) when the source is viewed edge-on. This is because the emission is optically thick (see Sect. 8.4.3), and hence the larger the emitting area, the higher the emission.

The effect of the viewing angle was considered by calculating the emission line for the fiducial envelope-only and envelope-plus-disk models and those with high mm opacity dust (i.e., large grains) with different viewing angles. Figure 8.B.3 presents the integrated methanol flux for these models. This figure shows that the integrated flux only changes by a factor smaller than 2 when the viewing angle is changed. Therefore, we consider a face-on view for the rest of this work.

8.3.2.1   Effects of envelope mass and luminosity

We focus on comparing the total warm methanol mass and the (continuum-subtracted) integrated methanol flux in various models. The warm methanol mass is defined as the methanol mass inside the snow surface. More quantitatively, where methanol abundance is higher than 10^{-9} in the envelope and higher than 10^{-11} in the disk. Figure 8.8 compares the warm methanol mass and its emission from different models with varying luminosity and envelope mass (or accretion rate).

For the warm methanol mass, the general trend is that with increasing envelope mass and luminosity, the warm methanol mass also increases. This is the same as was found by Nazari et al. (2022b) for the low-mass protostars. When the envelope mass increases, the warm methanol mass increases simply because there is more mass. When the luminosity increases, the warm methanol mass increases because the regions with temperatures above $68\,\mathrm{K}$ (methanol sublimation temperature at the densities of our models) become larger. The slope of this relation with luminosity agrees well with the analytical formula of warm mass being proportional to $L^{3/4}$ (see the solid gray line in Fig. 8.8; Nazari et al. 2021; van Gelder et al. 2022b).

The warm methanol mass in Fig. 8.8 is almost identical in the various models with the same luminosities and envelope masses (i.e., the models with or without a disk and those with high or low mm opacity dust). This is because the temperature structures are similar in most models with and without a disk and in those with low or high mm opacity dust, as explained in Sect. 8.3.1.1 (also see Fig. 8.2). Moreover, as shown in Fig. 8.7, there are almost no regions in which methanol is photodissociated to decrease the warm methanol mass for the fiducial models and those with high mm opacity dust. This was different for the low-mass protostellar models with M_{E} of $1\,\mathrm{M_\odot}$ (Nazari et al. 2022b), where larger photodissociation regions decreased the warm methanol mass.

There are slight variations (factor of $\lesssim 2$) between the warm methanol mass of models with low and high mm opacity dust grains or those with and without a disk (e.g., when $M_{\mathrm{E}} = 50\,\mathrm{M_\odot}$). The reason for these differences is the balance between various effects. Viscous heating in the disk becomes more effective when the accretion rate (or envelope mass) is higher. Therefore, colder disks are ex-
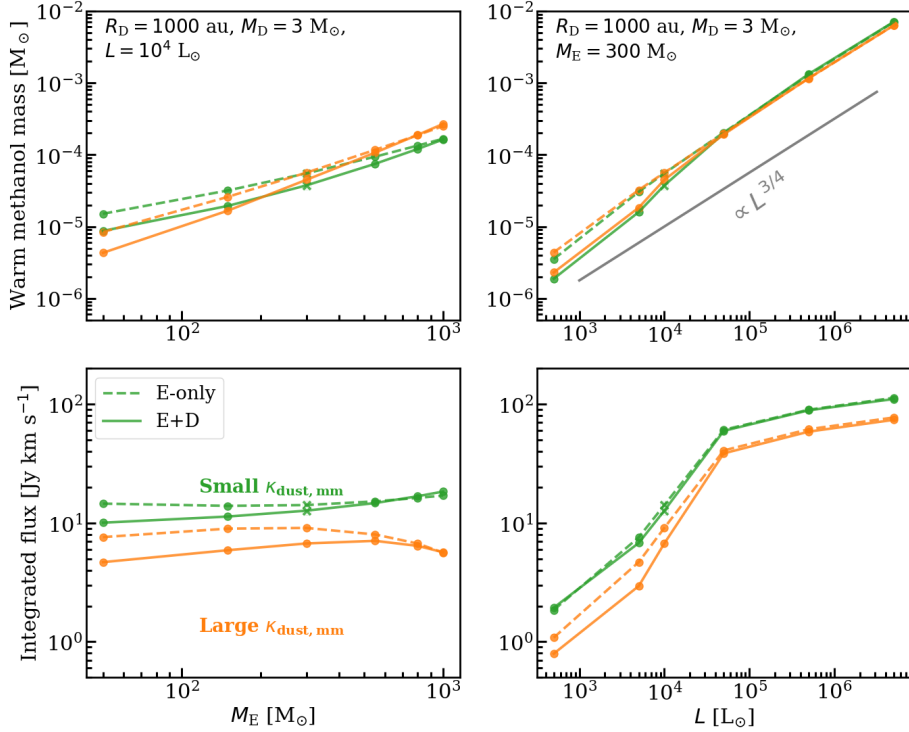
Figure 8.8: Warm methanol mass (top row) and integrated line fluxes (bottom row) for various models. The left column presents the models with varying envelope masses but constant luminosity of $10^4 \, L_\odot$ (i.e., varying accretion rates for the envelope-plus-disk models). The right column shows the models with varying bolometric luminosity but constant envelope mass of $300 \, M_\odot$ (i.e., constant accretion rate of $2 \times 10^{-3} \, M_\odot \, yr^{-1}$). The parameters that were fixed for each column are printed in the top row plots. For example, where the envelope mass was varied, the disk radius was fixed to 1000 au, the disk mass was fixed to $3 \, M_\odot$, and the luminosity was fixed to $10^4 \, L_\odot$. Orange and green show the models with high and low mm opacity dust. The fiducial models are indicated by a cross. Solid and dashed lines present the envelope-plus-disk and envelope-only models, respectively. The solid gray line in the top right panel shows the analytical relation of warm methanol mass and luminosity, which goes as $\propto L^{3/4}$ (van Gelder et al. 2022b). This relation is normalized by an arbitrary value here, hence, only its slope should be compared with the models. The integrated line fluxes were calculated after the lines were continuum subtracted, and a source distance of 4 kpc was assumed.

Figure 8.9: Comparison of methanol integrated fluxes between low- and high-mass protostars. The values for low-mass protostars are taken from Nazari et al. (2022b). The circles show the ratio of methanol-integrated fluxes of fiducial envelope-plus-disk models with varying luminosity to those of envelope-only models for high-mass protostars. The stars show the same for low-mass protostars. Green shows low mm opacity dust, and orange shows high mm opacity dust. Low-mass disks are more effective in decreasing the methanol emission than high-mass disks.
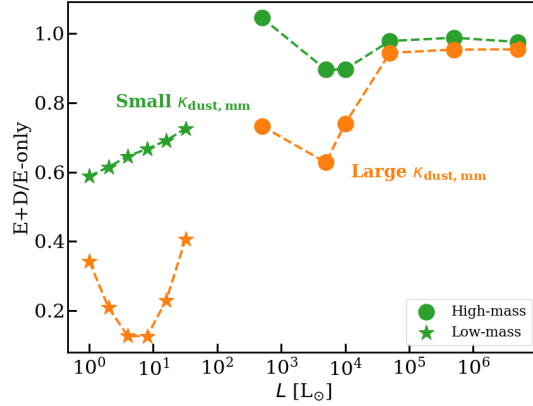
pected for models with lower envelope masses (and consequently, lower accretion rates). For example, for the lower end of envelope masses (i.e., $50\,M_\odot$ or $150\,M_\odot$), the envelope-plus-disk models are colder than the envelope-only models (see Figures 8.B.4 and 8.B.5). Moreover, the depth of UV penetration in the envelope also affects the warm methanol mass. In Fig. 8.B.4 (where $M_E = 50\,M_\odot$) large photodissociation regions are seen when the dust has a high mm opacity and a low UV opacity. This is especially important for lower envelope masses (i.e., lower densities), where it is easier for the UV to penetrate the envelope, photodissociate the methanol, and decrease the warm methanol mass.

The general trends seen in the warm methanol mass (top row of Fig. 8.8) is reflected in the integrated continuum-subtracted methanol line fluxes (bottom row), especially for the trends seen with respect to luminosity. The integrated fluxes are mainly flat for various envelope masses but increase with luminosity. Moreover, when the dust grains have a high mm opacity, the integrated line fluxes are always lower than when the grains have a low mm opacity (by factors of between about 2 and about 5), regardless of similar warm methanol masses (within factors of about 2) in most models: When the grains have a high mm opacity, they can block the methanol emission in the envelope or hide it in the disk through the continuum oversubtraction effect (see Sect. 4.1 of Nazari et al. 2022b for the explanation of this effect).

It is notable that for the luminosities, envelope masses, and disk radii in Fig. 8.8, high mm opacity dust in the envelope and the continuum oversubtraction effect decrease the integrated fluxes by factors between about 2 and 5. However, it does not show a significant decrease (i.e., about one order of magnitude) in methanol emission, as was seen in low-mass protostars (Nazari et al. 2022b). The difference between the effect of disk on methanol emission in low- and high-mass protostars is presented in Fig. 8.9. This figure shows that the methanol emission for the models with a disk and those without one are similar for high-mass protostars in

this work. More quantitatively, the ratio of emission in the two models is between $\sim$0.6 and $\sim$1 (a difference smaller than a factor of 2). In contrast, the methanol emission for the low-mass models can be dropped by a factor of $\sim$10 when disk and high mm opacity dust are included (Nazari et al. 2022b).

Finally, it is important to note that the methanol emission is optically thick (see Sect. 8.4.3). This can also be deduced by comparing the variations in warm methanol and those in integrated flux. The warm methanol mass varies by $\sim 3-4$ orders of magnitude as a function of envelope mass and luminosity, while the integrated flux spans a range of $\sim$2 orders of magnitude as a function of luminosity and only a range of factor $\sim$2 as a function of envelope mass. In addition to the fact that the warm methanol mass increases as a function of luminosity, the reason that an increase is seen in integrated flux for the models with more optically thick methanol lines is the larger emission area. If the line is optically thick, methanol emission would be proportional to the emitting area, and the higher the luminosity, the larger the methanol-emitting area (see Fig. 8.B.6 for the temperature structure of various models).

8.3.2.2 Effects of disk size

Figure 8.10 presents the variation of warm methanol mass and its emission with disk radius for three different luminosities. The warm methanol mass in all models is constant and is not a function of disk size. Moreover, the warm methanol mass is similar in the models with and without disk. This is because of the similar temperature structures, as explained in Sect. 8.3.1.1.

The methanol emission does not show a relation with disk radius either when the dust has a low mm opacity. There is a factor of at most 2 between the envelope-only models with high and low mm opacity dust. However, when the dust has a high mm opacity, the emission decreases with increasing disk size. Large disks cause a large (factor of at most $\sim$5) drop in integrated flux of the envelope-plus-disk model compared with the envelope-only model with high mm opacity dust.

A disk with a minimum radius of $\sim$1000 au and high mm opacity dust is necessary for a drop of at least a factor of about 2 in methanol emission compared with the envelope-only and envelope-plus-disk models with low mm opacity dust (at $L = 10^4 \, \mathrm{L}_\odot$). Moreover, for a drop of one order of magnitude, a disk size of $\sim 2000-2500$ au with high mm opacity dust is needed. These large drops are due to the continuum oversubtraction effect in the disk (see Fig. 8.B.7). In addition, the radius at which a drop is seen in methanol emission in the disk-plus-envelope models increases with luminosity. In other words, larger disk sizes are needed for a large decrease in methanol emission if a source has a high luminosity.

8.4   Discussion

8.4.1   Comparison with observations

The main goal of this work is to examine whether it is possible to explain the spread in observations of methanol emission discussed in van Gelder et al. (2022b).
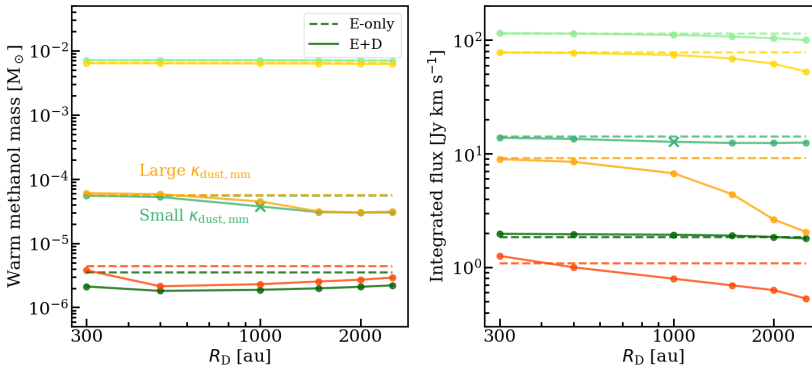
Figure 8.10: Warm methanol mass (left column) and integrated methanol emission (right column) for various disk sizes. The various shades of green and orange are used to indicate variations in luminosity. The luminosity from low to high is indicated by the darkest to lightest color. The models plotted here have luminosities $5 \times 10^2 \, L_\odot$, $1 \times 10^4 \, L_\odot$ and $5 \times 10^6 \, L_\odot$. The dashed lines present fiducial envelope-only models with various luminosities. The solid lines present the fiducial envelope-plus-disk models with various luminosities and disk radii. The shades of orange show models with large dust grains (high mm opacity), and the shades of green show those with small grains (low mm opacity).

Therefore, we compare in this section the integrated flux of methanol from the models with that of the same methanol line in ALMAGAL observations (CH_3OH $4_{2,3,1}$-$3_{1,2,1}$, $\nu = 218.4401 \, \mathrm{GHz}$, $E_{up} = 45.5 \, \mathrm{K}$ and $A_{i,j} = 4.7 \times 10^{-5} \, \mathrm{s}^{-1}$) from van Gelder et al. (2022b).

Figure 8.11 presents the comparison of our models with observations. First, the scaling of flux with luminosity in our models and the data is apparent, as also explained in Sect. 8.3.2.1. Second, the regions indicating envelope-only and envelope-plus-disk models with low mm opacity dust grains (red and blue smooth regions) coincide. This is expected from the similar temperature structures and warm methanol masses between the two models, as discussed in Sections 8.3.1.1 and 8.3.2. Third, the integrated fluxes from the two models when the grains have a high mm opacity are also similar, with the envelope-plus-disk models having integrated fluxes that are a factor of about 2 to 3 lower when the luminosities are below about $10^4 \, L_\odot$ due to continuum oversubtraction. Finally, the models cannot explain the whole range ($\sim$2 orders of magnitude) of methanol emission. Although they fail to match the observations with integrated methanol fluxes below $\sim$0.1 Jy km s^{-1}, they do explain the data better when the luminosities are lower. The models especially miss the data points at higher luminosities ($L \simeq 10^4 - 10^5 \, L_\odot$).

This shows that disks and dust optical depth effects are not as effective in massive protostars in decreasing the methanol emission as the low-mass protostars studied in Nazari et al. (2022b), where disks could explain the spread in observations well. Although they can explain the spread of almost two orders of
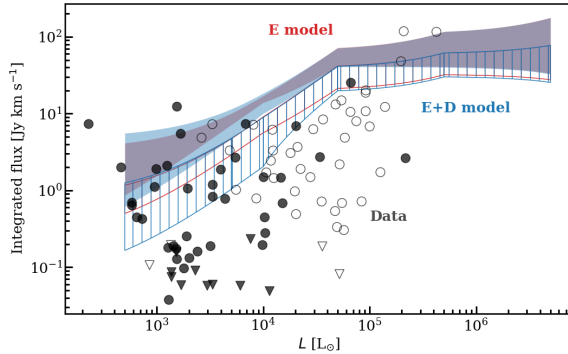
Figure 8.11: Comparison of models with observations of ALMAGAL sources. The same methanol line is used for the models and observations. Moreover, the integrated fluxes from the observations are normalized to a distance of 4 kpc to match those from the models. The black data points present the observations, where the circles are detections and triangles are upper limits. The empty symbols indicate sources whose L/M from Elia et al. (2017) is above $22.4 \, \mathrm{L_\odot \, M_\odot^{-1}}$, proposed to be 'HII region candidates'. The smooth red and blue regions show the results from the envelope-only and envelope-plus-disk models with low mm opacity dust grains. The striped regions show the same for models with high mm opacity dust. The regions into which the models fall (blue and red) are found by simply connecting the integrated fluxes at the six different luminosities considered in this work in linear space.

magnitude in methanol emission at low luminosities ($\sim 5 \times 10^2 \sim 10^4 \, \mathrm{L_\odot}$), they cannot explain the data at higher luminosities. Therefore, other effects are needed, which are discussed further below.

8.4.2   Alternative explanations

8.4.2.1   Larger disk sizes and lower envelope masses

One way to further lower the methanol emission is to increase the disk radii in our models (see Fig. 8.10). This is not realistic because disks become more unstable as they become larger and more massive.

The disks considered here are stable by definition from the calculation of Toomre Q parameter. We calculated the Toomre Q parameter for our disks, but because the disk masses and the disk radii are changed such that $M_\mathrm{D}/R_\mathrm{D}^2$ always stays equal to $0.003 \, \mathrm{M_\odot \, R_\odot^{-2}}$, our disks are always stable by definition. However, the maximum disk radius of 2500 au in our models is the most extreme limit on the disk radius in massive protostars from observations (e.g., see Jiménez-Serra et al. 2012; Hunter et al. 2014; Zapata et al. 2015; Williams et al. 2022). We especially note that it is easier to observe the larger and more massive disks, which means that if disks larger than $\sim$2500 au have not yet been observed, it might be an indication that they do not exist.

Many of the observations of large disks or rotating structures (referred to as

toroids; see Beltrán & de Wit 2016) show evidence of fragmentation when they are observed with higher angular resolution (e.g., Beuther et al. 2009; Beuther et al. 2017; Ilee et al. 2016; Ilee et al. 2018; Beuther et al. 2018; Suri et al. 2021). One of the best-studied large Keplerian disks known to date is that around the protostar AFGL 4176, which was found to have a radius of 2000 au (Johnston et al. 2015; also see Bøgelund et al. 2019a for the extent of emission from various species). Recently, Johnston et al. (2020) used even higher angular resolution data of this disk to calculate the Toomre Q parameter. They concluded that the outer part of the disk is unstable and is prone to fragmentation. Therefore, disks larger than 2500 au are not realistic, and we cannot simply increase the disk radius to explain the whole range of methanol emission observed in Fig. 8.11.

Another parameter that can be changed to decrease the methanol emission is the envelope mass (see Fig. 8.8). This is because the lower the envelope mass, the lower the warm methanol mass and hence the lower the methanol emission, especially because the emission will become more optically thin toward this end. The ranges of envelope masses observed for high-mass protostellar systems, especially those shown in Fig. 8.11, are mostly above $50\,\mathrm{M}_\odot$ (van der Tak et al. 2000; Schuller et al. 2009; Dunham et al. 2011; Elia et al. 2017; König et al. 2017). Therefore, it is not a realistic solution to decrease the mass in order to decrease the methanol emission.

8.4.2.2 Absence of methanol

This section considers the case when the abundance of methanol in some high-mass systems is intrinsically lower. One way to have less methanol is to have large HII regions from which methanol is absent. As explained in Sect. 8.2.1 HII regions are not included in our models. A self-consistent modeling of the HII region, including its extent, is beyond the scope of the paper. However, it is expected that ∼40% of the emitted photons of a star with a blackbody radiation at $T_\star = 40000\,\mathrm{K}$ have higher energies than the energy needed to ionize hydrogen.

We explored how the methanol emission would change if we included spheres with various radii from which methanol is absent in our fiducial envelope-only model (see Fig. 8.12). These spheres were to mimic the effect of a potential HC or UC HII region in a protostellar system. We assumed no methanol in the HII regions because the gas is atomic and ionized in these regions by definition. The radii considered for the spheres without methanol inside were 50 au, 200 au, 500 au, 1000 au, 5000 au, and 10000 au. The values assumed here are in line with the extents suggested by modeling and observational works for HC or UC HII regions (Keto 2003; Sewilo et al. 2004; Hoare et al. 2007; Cyganowski et al. 2011; Sánchez-Monge et al. 2013a; Ilee et al. 2016; Williams et al. 2022). We note that sources with disks can also have an HII region related to the disk wind (Hollenbach et al. 1994), but modeling these disk winds is beyond the scope of this paper. The effect of HII regions on methanol emission was therefore only considered in the envelope-only models, whose methanol fluxes are similar to those of models with disks (see Fig. 8.11).

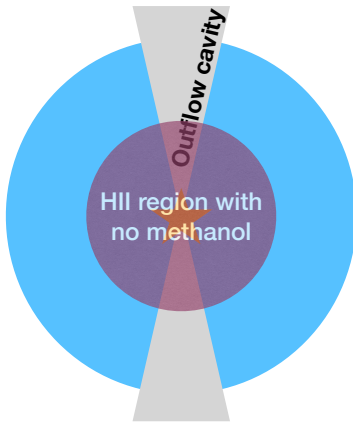Figure 8.13 presents the warm methanol mass and integrated line fluxes for

Figure 8.12: Sketch of the potential HC or UC HII region around a high-mass protostar. It is expected that methanol is absent in this region as the gas is atomic and ionized.

the fiducial envelope-only models with different assumed HC or UC HII region sizes above 500 au (those with assumed HII region sizes smaller than or equal to 500 au are shown in Fig. 8.B.10). The warm methanol mass does not change significantly compared with the fiducial envelope-only model (see Fig. 8.8) for most models with $L \gtrsim 10^4 \, \mathrm{L_\odot}$ and an HII region size of 1000 au. Moreover, the integrated methanol flux does not change significantly compared with the fiducial envelope-only model for all luminosities when the carved HII region is ≤ 1000 au (also see Fig. 8.B.10). However, when the carved region has a size of ≥ 5000 au, the warm methanol mass and methanol emission drop. More quantitatively, the methanol emission is decreased by ~ 1 order of magnitude when the carved region is 5000 au and the the luminosities are $\lesssim 10^4 \, \mathrm{L_\odot}$. The integrated flux decreases even more (by $\gtrsim 2$ orders of magnitude) for all luminosities when the HII region is 10000 au. This shows that for a large drop in methanol emission such that the models match the data in Fig. 8.11, an HII region of size of > 5000 au is needed. These sizes would fall into the category of a large HC HII region or an UC HII region.

Elia et al. (2017) categorized the sources with $L/M > 22.4 \, \mathrm{L_\odot} \, \mathrm{M_\odot^{-1}}$ as 'HII region candidates', where HII region here mainly means ultracompact or compact HII regions (also see Cesaroni et al. 2015). Therefore, the sources that satisfy this criterion based on the luminosities and masses given by Elia et al. (2017) are highlighted in Fig. 8.11 by empty symbols. It is interesting that almost all the sources with luminosities between $10^4 \, \mathrm{L_\odot}$ and $10^5 \, \mathrm{L_\odot}$ might be HII region candidates. Hence, the data in that part of the plot can be explained by those sources having an UC or compact HII region. We note that if a source hosts a HC or UC HII region, it is not guaranteed that the methanol emission is low. This only occurs if the HII region is large enough compared with the methanol sublimation region (also see Fig. 8.13). However, if methanol emission is low, it is important to consider the potential effects from a HC or UC HII region.

It is not clear why some sources with luminosities between $10^3 \, \mathrm{L_\odot}$ and $10^4 \, \mathrm{L_\odot}$ have lower methanol emission than our models. Another way to decrease the methanol abundance in a protostar could be its destruction by X-rays. It has re-
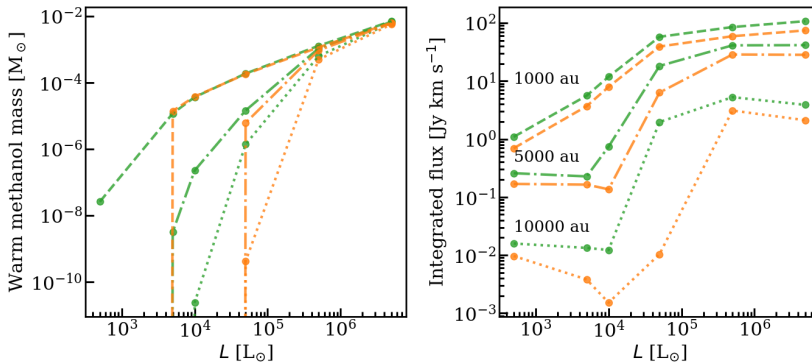
Figure 8.13: Warm methanol mass (left) and integrated line flux of methanol (right) for envelope-only fiducial models with different luminosities and carved HC or UC HII regions. Green and orange show low and high mm opacity dust models. Dashed lines show when the size of HII region is 1000 au, dashed dotted lines show the same for 5000 au, and the dotted lines show the same for 10000 au. An HII region of size ∼10000 au is needed for a drop of $\gtrsim 2$ orders of magnitude in methanol emission.

cently been found that X-rays can cause lower methanol emission in low-mass protostars (Notsu et al. 2021). In particular, they find that for $L_{\mathrm{X}} \gtrsim 10^{30} - 10^{31}\,\mathrm{erg\,s^{-1}}$, the methanol abundance decreases significantly. Stäuber et al. (2005) considered X-ray chemistry for high-mass protostars and reported an X-ray luminosity $\gtrsim 10^{31}\,\mathrm{erg\,s^{-1}}$ for the high-mass source AFGL 2591. Based on these results and those of Notsu et al. (2021), methanol in high-mass protostars similar to AFGL 2591 could be destroyed by X-ray chemistry in the envelope. However, whether this phenomenon is important is still to be confirmed, especially because Benz et al. (2016) found no evidence of X-ray chemistry in a sample of low- and high-mass protostars on scales of ∼1000 au.

If the study of Notsu et al. (2021) can be applied to high-mass protostars, it is expected that HCO^+ is abundant on-source when methanol is not detected or its flux is low. That is, because X-rays also destroy water (Notsu et al. 2021) and where water is absent, HCO^+ is abundant (van 't Hoff et al. 2022). Therefore, to solve the mystery of low methanol emission in massive protostars with luminosities between $10^3\,\mathrm{L_\odot}$ and $10^4\,\mathrm{L_\odot}$ in Fig. 8.11, high spatial resolution studies with deep observations of HCO^+ and its isotopologs in these sources are needed.

Finally, it is also possible that methanol simply forms less efficiently toward massive protostars because of their potentially warmer prestellar phase. This would agree with observations of van Gelder et al. (2022a), who measured lower D/H ratios toward massive protostars compared with their low-mass counterparts. They interpreted their results as either a warmer prestellar phase or shorter prestellar lifetimes for these massive sources compared with low-mass protostars. However, if this is the case, we would expect that it would happen for all the sources in Fig. 8.11 and affect them all similarly. Therefore, the reason for low methanol emission of some sources is probably not the low production rate of this molecule.

8.4.3 Caveats

One important fact about the methanol emission in our models is that it is optically thick. This was already pointed out in Sect. 8.3.2.1, where the integrated methanol emission spans a smaller range than the warm methanol mass (Fig. 8.8). This can be confirmed by calculating the line optical depth in the fiducial models. Figure 8.B.8 presents a radial cut through the line optical depth in the fiducial envelope-only and envelope-plus-disk models. This figure shows that the emission is optically thick inside the methanol snow surface for these two models.

Because the line is already optically thick (the emission is proportional to the emitting area), increasing the abundance of methanol in the inner and outer disk by two orders of magnitude (based on the findings of Bøgelund et al. 2019a) should not change the integrated emission significantly. Therefore, we specifically tested this for the fiducial envelope-plus-disk model. The line emissions are shown in Fig. 8.B.9. The integrated flux is only $< 1\%$ higher when the abundance is higher. Therefore, the conclusions made here should not change when higher methanol abundances are assumed in the disk as long as optically thick methanol lines are considered. Moreover, we tested a case in which the methanol abundance in the disk is one order of magnitude lower than assumed in this work. Again, the integrated methanol flux is only $< 1\%$ lower when the methanol abundance is lower. Therefore, this cannot be the reason for the low methanol emission in the observations.

Another assumption is the protostellar mass and temperature. A few models with a stellar temperature of $20000\,\mathrm{K}$ and a stellar mass of $10\,\mathrm{M_\odot}$ were run to test the effect. However, the change in the integrated methanol flux was smaller than a factor ~ 1.5.

We did not include the effect of shocks in enhancing the methanol emission in our models. Studies showed that shocks can enhance the abundance of various molecules, including methanol (Csengeri et al. 2019; van Gelder et al. 2021; Garufi et al. 2022). Therefore, including this effect of shocks would increase the methanol emission and would separate the models even more from observations in Fig. 8.11.

Finally, we made the assumption that the hydrogen-ionizing photons from the protostar are reemitted at a longer wavelength (assumed to be Lyman-α here) before they interact with the dust. In reality, the photons can be emitted at longer wavelengths via a forest of lines from atomic and ionized species. Hence, we considered a case in which these ionizing photons were completely eliminated from the system, representing a lower limit on methanol emission. The reality is more similar to the main grid run in this paper in terms of including these photons. When the ionizing photons are deleted in the fiducial envelope-only and envelope-plus-disk models, the integrated methanol emission is only a factor of $\lesssim 2$ lower than the models considered here. Therefore, the large spread seen in the data cannot be explained by a change in the exact spectrum emerging from the HII region surrounding the protostar.

8.5   Conclusions

We considered the importance of disks in decreasing methanol emission in high-mass protostars. We studied two models: an envelope-only model, and an envelope-plus-disk model. Both models include low and high mm opacity dust grains separately (representing small and large grains). A wide range of parameters were considered in envelope-only and envelope-plus disk models. The luminosities range from $5 \times 10^2 \, L_\odot$ to $5 \times 10^6 \, L_\odot$, envelope masses from $50 \, M_\odot$ to $1000 \, M_\odot$ and disk radii from $300 \, au$ to $2500 \, au$. Our conclusions are summarized below.

- The temperature structures of high-mass protostellar systems with and without a disk are similar. This is because the disk midplane is hot due to viscous heating in the disk and disk shadowing is not as effective as it is for low-mass protostellar disks. Moreover, the temperature structures of models with low and high mm opacity are also similar. The warm methanol mass is hence similar in these models because the temperature structures are similar.

- Dust with high mm opacity blocks the methanol emission in the envelope and hides it in the disk through the continuum oversubtraction effect. The minimum disk size to observe a drop of a factor of two between the envelope-only models with small grains (low mm opacity) and the envelope-plus-disk models with large grains (high mm opacity) increases with luminosity. At $L = 10^4 \, L_\odot$, this disk size is ${\sim}1000 \, au$. For a drop of an order of magnitude in emission at $L = 10^4 \, L_\odot$, a minimum disk size of ${\sim}2000 - 2500 \, au$ is needed.

- The temperature-inversion effect that was suggested by Barr et al. (2020) in the disk to explain the absorption lines toward two massive protostars is indeed found in our models at $50 \, au$, but only in models with high mm opacity dust. This effect is only observed when the envelope mass is $\gtrsim 550 \, M_\odot$ or when the accretion rate is $\gtrsim 3.6 \times 10^{-3} \, M_\odot \, yr^{-1}$.

- The entire spread in observed methanol emission toward high-mass protostars (especially sources with high luminosities higher than ${\sim}10^4 \, L_\odot$) cannot be explained by the presence of a disk or dust opacity. This is in contrast with models by Nazari et al. (2022b) for low-mass protostars. A possible explanation for low methanol emission of sources with high luminosities could be that they host a HC or UC HII region, as also suggested by their L/M ratio.

The lowest methanol emission in low-luminosity objects ($L \simeq 10^3 - 10^4 \, L_\odot$) might be due to destruction of methanol by X-rays in these sources. Hence, these object are prime targets for studying X-ray chemistry. A future step is to study these sources with deep and higher angular resolution observations.

Appendix

8.A   Passive heating versus viscous heating

The analytical solution for the temperature in the midplane from passive heating can be given by (Chiang & Goldreich 1997; Dullemond et al. 2001; Dullemond et al. 2018)

$$T_{\mathrm{mid,irr}} = \left(\frac{0.5\varphi L}{4\pi R^2 \sigma_{\mathrm{SB}}} \right)^{1/4}, \tag{8.6}$$

where σ_{SB} is the Stefan–Boltzmann constant, and φ is the flaring angle. Here, φ is assumed to be 0.2 to match the temperatures found from RADMC-3D models in the outer radii (see the left panel of Fig. 8.3). This equation is a result of balancing heating from the star and cooling. The heating from the star strongly depends on the geometry and on the angle at which the radiation impinges on the disk.

We know that the dissipated power per unit area due to viscosity is given by $\sigma_{\mathrm{SB}} T_{\mathrm{surf,visc}}^4$. The temperature that this dissipated energy corresponds to is then (Lodato 2008)

$$2\sigma_{\mathrm{SB}} T_{\mathrm{surf,visc}}(R)^4 = \int_{-\infty}^{\infty} Q(R,z)dz = \frac{3\dot{M}}{4\pi} \frac{GM_\star}{R^3} \left(1 - \sqrt{\frac{R_{\mathrm{in}}}{R}} \right). \tag{8.7}$$

Factor 2 on the lefthand side of this equation comes from the fact that a disk has two sides. This is the analytic approximation of disk surface temperature from viscous heating. However, as explained in Sect. 8.3.1.1, the midplane temperature is hotter than the surface layers because the densities are higher and hence the optical depth in the midplane is higher. The midplane temperature can be approximated by (Armitage 2010)
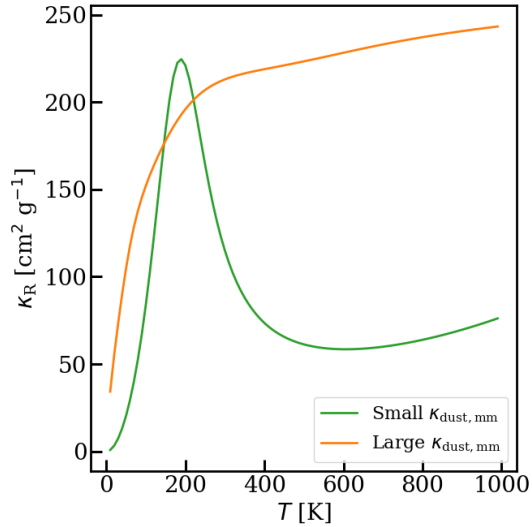
Figure 8.A.1: Rosseland mean opacity as a function of temperature.

$$T_{\mathrm{mid,\,visc}}^4 \simeq \frac{3}{4}\tau T_{\mathrm{surf,visc}}^4, \tag{8.8}$$

where $\tau = \kappa_{\mathrm{R}}\Sigma_{\mathrm{dust}}/2$ and κ_{R} is the Rosseland mean opacity. The Rosseland mean opacity can be calculated using

$$\frac{1}{\kappa_{\mathrm{R}}} = \frac{\int_0^{\nu'} \frac{1}{\kappa_\nu}\frac{dB_\nu(T)}{dT}d\nu}{\int_0^{\nu'} \frac{dB_\nu(T)}{dT}d\nu}, \tag{8.9}$$

where κ_ν is the absorption opacity, and $B_\nu(T)$ is the Planck function. The integrals are calculated for ν going from zero to ν', where ν' is assumed to be the frequency of the photons that can ionize hydrogen (the wavelength of these photons would be $\sim 0.1\,\mu$m). Equation (8.9) is dependent on the temperature. To calculate κ_{R}, an initial temperature of $T_{\mathrm{surf,visc}}$ from Eq. (8.7) is therefore assumed to give an initial value of κ_{R}. This initial value is then used to find the temperature from Eq. 8.8. This procedure is performed iteratively until κ_{R} varies by less than 0.01 from one iteration to the next. Figure 8.A.1 shows the resulting κ_{R} as a function of temperature. In reality, the total heating in the disk midplane ($\propto T_{\mathrm{mid,total}}^4$) is the sum of the heating from viscosity and radiation from the star. Therefore,

$$T_{\mathrm{mid,total}}^4 \simeq \frac{3}{4}\tau T_{\mathrm{surf,visc}}^4 + T_{\mathrm{mid,irr}}^4. \tag{8.10}$$

In a similar way, the disk surface temperature can be derived. The disk surface temperature ($T_{\mathrm{surf,visc}}$) due to viscosity can be found from Eq. (8.7). The temperature in the disk surface due to passive heating is given by (Dullemond et al. 2001)

$$T_{\text{surf,irr}} = \left(\frac{L}{\epsilon 8\pi\sigma_{\text{SB}}R^2}\right)^{1/4},\tag{8.11}$$

where $\epsilon = \kappa_{\text{P}}(T_{\text{surf,irr}})/\kappa_{\text{P}}(T_\star)$. Moreover, κ_{P} is the Planck mean opacity, given by

$$\kappa_{\text{P}} = \frac{\int_0^{\nu'}\kappa_\nu B_\nu(T)d\nu}{\int_0^{\nu'} B_\nu(T)d\nu}.\tag{8.12}$$

The Planck mean opacity, similar to the Rosseland mean opacity, is dependent on the temperature. Therefore, to calculate $\kappa_{\text{P}}(T_{\text{surf,irr}})$, the midplane temperature due to passive heating ($T_{\text{mid,irr}}$) is first used to find κ_{P} , and then this is used in Eq. (8.11) to find $T_{\text{surf,irr}}$, to be used again to calculate κ_{P}. This process is performed iteratively until the value of κ_{P} converges.

Finally, the heating in the disk surface ($\propto T_{\text{surf,total}}^4$) is the sum of the heating due to viscous heating and passive heating. In other words, it is given by

$$T_{\text{surf,total}}^4 \simeq T_{\text{surf,visc}}^4 + T_{\text{surf,irr}}^4.\tag{8.13}$$

8.B   Additional plots

Figure 8.B.1 is the same as Fig. 8.4, but for a bolometric luminosity of $5\times10^5\,\text{L}_\odot$ and a vertical temperature cut at 30 au. Figure 8.B.2 presents the methanol emission at the peak of the line viewed edge-on for the fiducial models. Moreover, this figure shows the line flux for the fiducial models. Figure 8.B.3 presents the effect of viewing angle on the integrated flux of the fiducial envelope-only and envelope-plus-disk models and those with high mm opacity dust. Figures 8.B.4 and 8.B.5 are the same as Fig. 8.7, but for envelope masses of $50\,\text{M}_\odot$ and $150\,\text{M}_\odot$, respectively. Figure 8.B.6 presents the temperature structure of envelope-only and envelope-plus-disk models for the various parameters we varied in this work. Figure 8.B.7 shows that continuum subtraction results in an error in the measured intensity for the fiducial model with high mm opacity and a disk radius of 2000 au. It particularly shows that the intensity of the continuum, line plus continuum, and line-only runs are all the same in the inner $\sim$1500 au. Figure 8.B.8 presents the optical depth of the methanol line as a function of radius for the fiducial envelope-only and envelope-plus-disk models viewed face-on. Figure 8.B.9 presents the methanol emission line for the fiducial envelope-plus-disk model and that with disk methanol abundances that are two orders of magnitude higher. Figure 8.B.10 presents the warm methanol mass and integrated methanol flux for models with a simulated HII region for the envelope-only models by setting the methanol abundance to zero in an inner sphere. The radii assumed for the inner sphere in Fig. 8.B.10 are 50 au, 200 au, and 500 au.
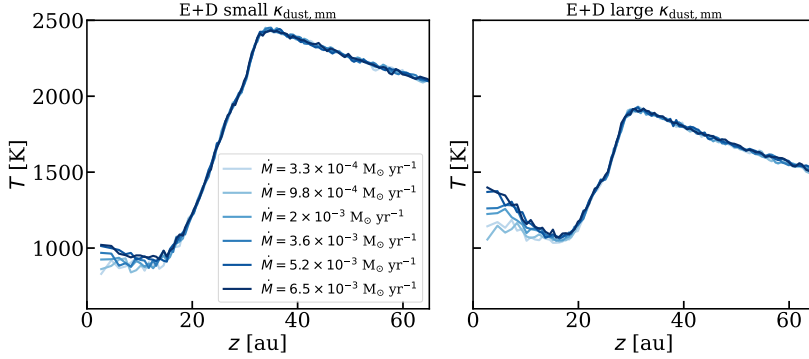
Figure 8.B.1: Same as Fig. 8.4, but when the bolometric luminosity is $5 \times 10^5 \, \mathrm{L_\odot}$ and the vertical temperature cut is made at 30 au.
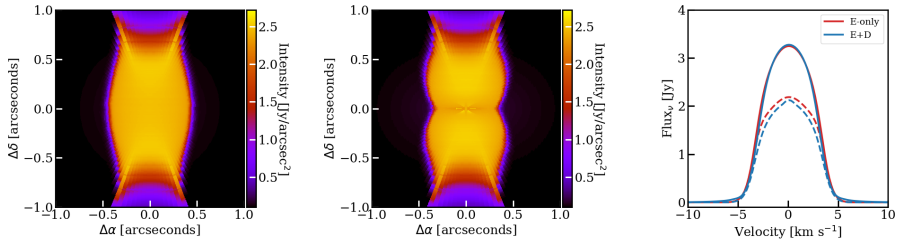

Figure 8.B.2: Methanol emission from the fiducial envelope-only and envelope-plus-disk models. The left and middle panels show the emission at the peak of the line viewed edge-on for the two models without dust in these two particular models, so that the methanol emission can be seen without optical depth effects from the dust (dust is included in all other models, unless otherwise stated). The right panel shows the continuum-subtracted line flux at an assumed source distance of 4 kpc when viewed edge-on (solid lines) and face-on (dashed lines).
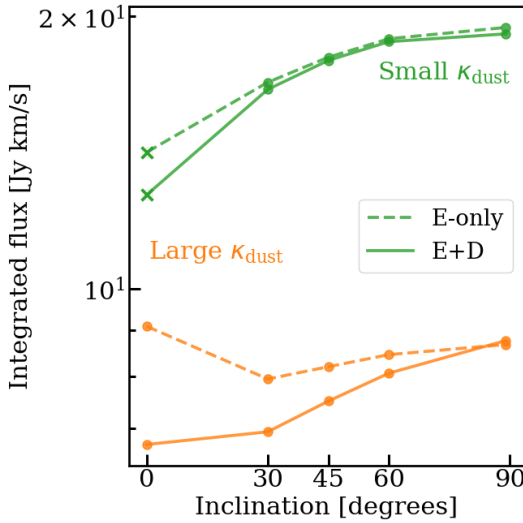
Figure 8.B.3: Integrated methanol flux as a function of viewing angle for the fiducial envelope-only and envelope-plus-disk models and for models with high mm opacity dust. The difference in integrated flux is smaller than a factor of 2 when the viewing angle changes.
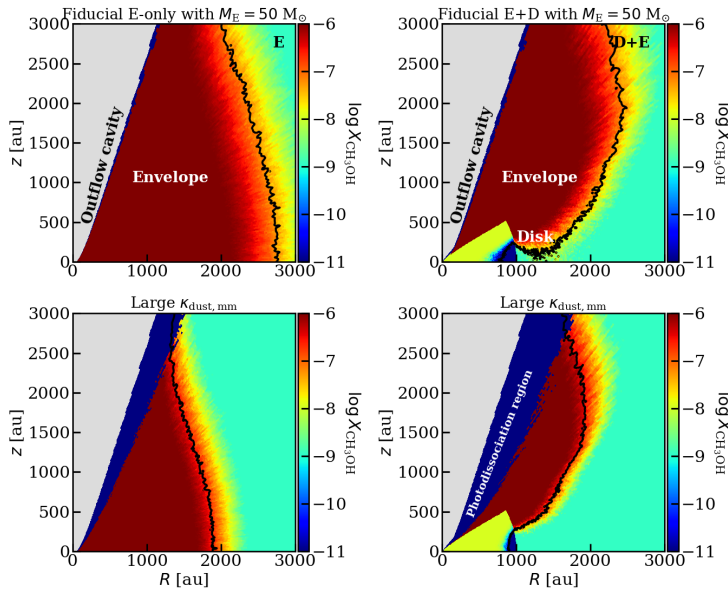

Figure 8.B.4: Same as Fig. 8.7, but now for $M_{\mathrm{E}} = 50\,\mathrm{M}_\odot$. The photodissociation regions for the models with high mm opacity dust are significant.
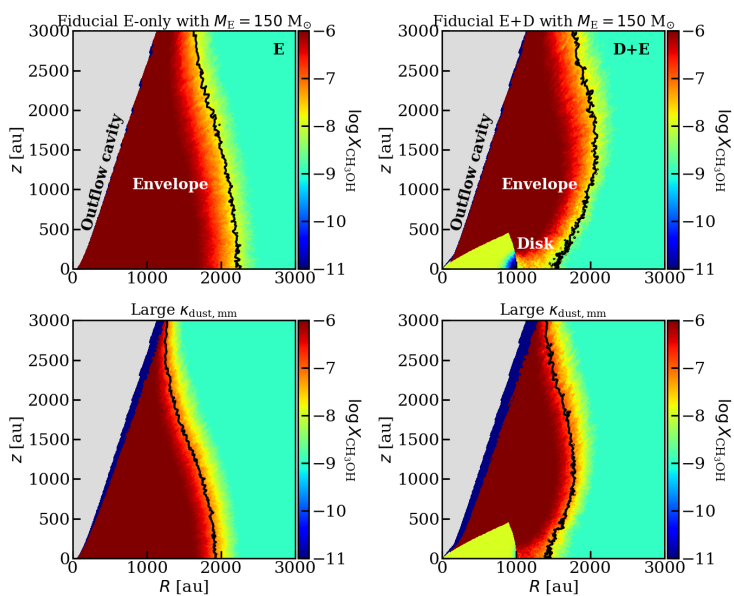
Figure 8.B.5: Same as Fig. 8.7, but now for $M_E = 150 \, M_\odot$.
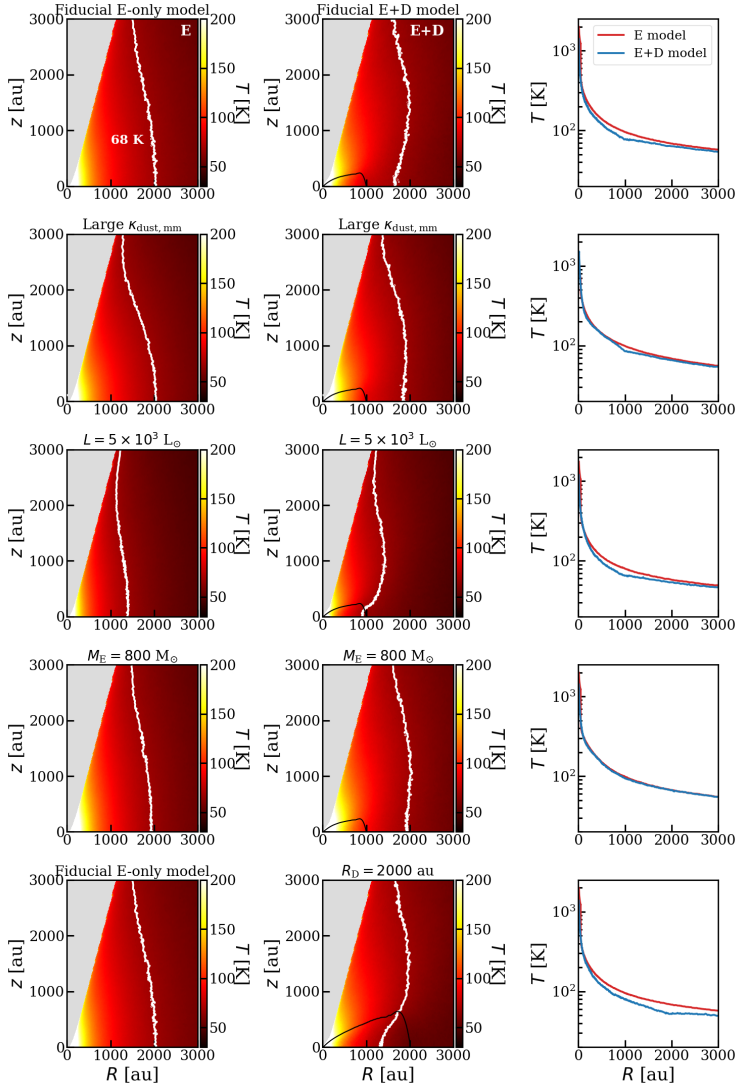
Figure 8.B.6: Temperature structure of models with different parameters. The left column presents the envelope-only models, the middle column shows the envelope-plus-disk models, and the right column presents the comparison of a temperature cut at $z = 0\,\mathrm{au}$ between the two models. The rows from top to bottom show the fiducial model, the model with high mm opacity dust, with a protostellar luminosity of $5 \times 10^3\,\mathrm{L_\odot}$, with an envelope mass of $800\,\mathrm{M_\odot}$, and finally, the fiducial model with a disk radius of $2000\,\mathrm{au}$.

Figure 8.B.7: Intensity cut through the fiducial model with high mm opacity dust and a disk radius of 2000 au. Orange shows the model when dust and gas are included in the run, blue shows the model when only dust is included, and green shows the model without dust. The intensity of the line, the continuum, and the continuum plus line in the inner ~1500 au are similar while continuum subtraction will result in almost zero intensities.
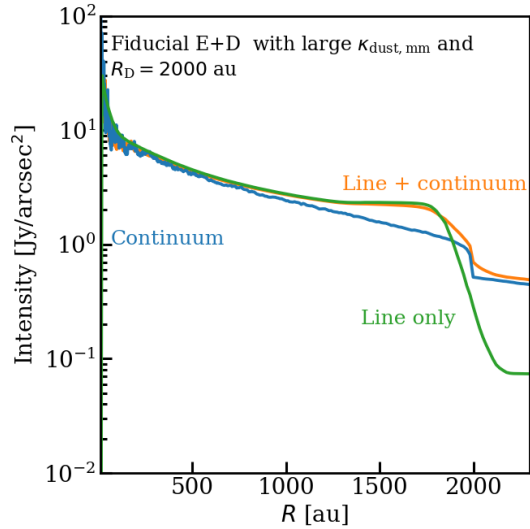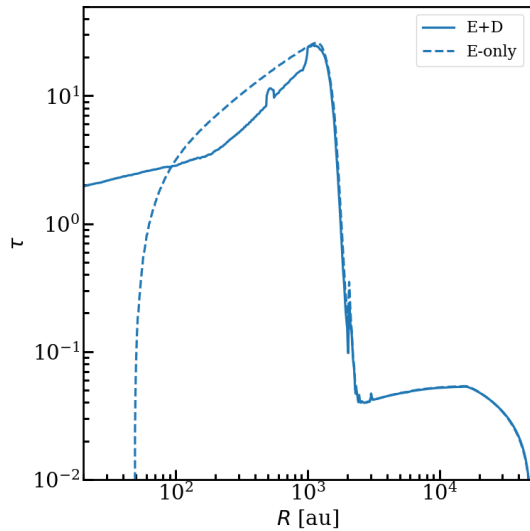

Figure 8.B.8: Methanol optical depth as a function of radius at the peak of the line. The dashed and solid lines show the fiducial envelope-only and envelope-plus-disk models, respectively. The emission is optically thick inside the snow surface.
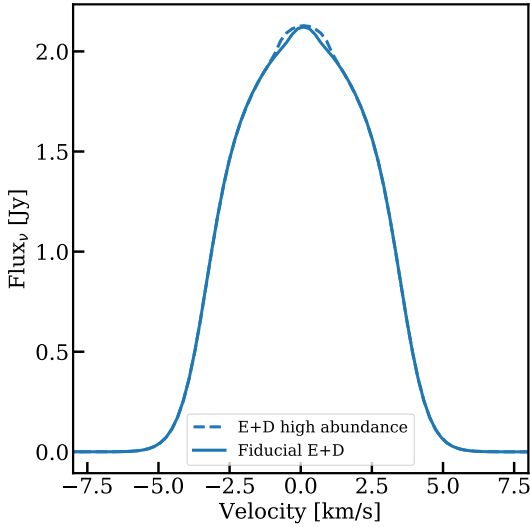
Figure 8.B.9: Methanol line emission for the fiducial envelope-plus-disk model (solid line) and the same with disk abundances that are two orders of magnitude higher (dashed line).
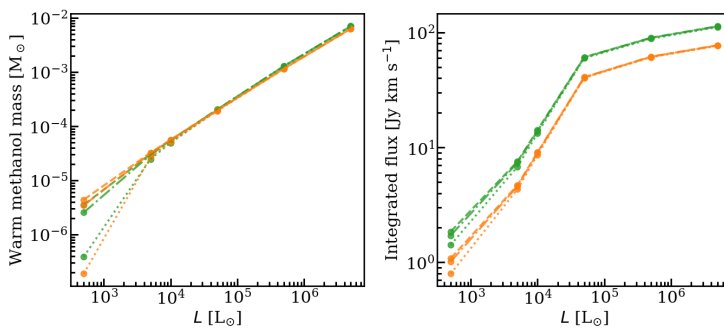

Figure 8.B.10: Same as Fig. 8.13, but dashed lines show the carved region with a size of 50 au, dash-dotted lines show the same for 200 au, and the dotted lines show the same for 500 au.